Laboratory chamber measurements of the longwave extinction spectra and complex refractive indices of African and Asian mineral dusts

C. Di Biagio[1], P. Formenti[1], S. A. Styler[2,3], E. Pangui[1], and J.-F. Doussin[1]

[1]LISA, UMR CNRS 7583, Université Paris Est Créteil et Université Paris Diderot, Institut Pierre Simon Laplace, Créteil, France, [2]Department of Chemistry, University of Toronto, Toronto, Ontario, Canada, [3]Leibniz Institute for Tropospheric Research, Leipzig, Germany

Abstract In this study we present the first results from laboratory chamber experiments newly designed to investigate the longwave optical properties of mineral dust. Extinction spectra in the 2–16 μm range have been measured in situ ($T = 293$ K, RH < 2%) for polydispersed pure dust aerosols generated from natural parent soils from Tunisia, Niger, and the Gobi desert. Data are used in combination with particle size distributions to estimate the complex refractive index of each dust sample. Our results show that the magnitude and spectral dependence of the dust extinction and refractive indices differ according to particle mineralogy, suggesting the necessity for regionally resolved optical properties for modeling dust radiative effects in the longwave. The magnitude of extinction is controlled by the particle size distribution and remains significant down to low coarse particle concentrations, indicating that the longwave effect of mineral dust persists throughout long-range transport and is thus relevant at the global scale.

1. Introduction

The interaction of large mineral dust particles with longwave radiation has been demonstrated to have important implications for climate and remote sensing applications. For instance, the warming effect due to the absorption of longwave radiation by dust particles counterbalances a significant fraction of the shortwave cooling, thus modulating the overall dust radiative impact [*Hsu et al.*, 2000; *Slingo et al.*, 2006; *di Sarra et al.*, 2011; *Haywood et al.*, 2011]. Dust also directly affects satellite observations by modifying the top-of-atmosphere longwave outgoing radiance spectrum [*Sokolik*, 2002], which in turn influences the satellite retrieval of several key climatic parameters, such as sea surface temperature and greenhouse gases concentration [*May et al.*, 1992; *Merchant et al.*, 2006].

Currently, large uncertainties persist in the quantification of the dust longwave radiative effect and its associated impacts. One of the main reasons for this is the very poor knowledge of the dust optical properties in this region of the spectrum [*Claquin et al.*, 1998; *Balkanski et al.*, 2007]. In particular, the sensitivity study of *Highwood et al.* [2003] has demonstrated that the complex refractive index ($m = n - ik$) is the dominant uncertainty when trying to reproduce, by calculations, the brightness temperature observed from measurements during dust events.

Dust optical properties in the longwave are strictly controlled by particle physicochemical properties (e.g., composition, size, and shape). Dust is composed of several minerals, such as clays (illite, kaolinite, smectite, chlorite), quartz, Ca-rich species (calcite, dolomite, gypsum), feldspars (orthose, albite), iron (hematite, goethite), and titanium oxides, each characterized by its own absorption features in the longwave [*Sokolik et al.*, 1998]. The spectral dependence of dust absorption properties depends on the relative abundance and state of mixing of these minerals, while the magnitude of the dust-radiation interaction is strongly modulated by their size distribution [*Sokolik and Toon*, 1999]. In addition, the band shape and position of resonant absorption peaks vary significantly with particle shape [*Laskina et al.*, 2012].

The composition, size, and shape of dust particles vary in space and time depending on the soil mineralogy of the specific source area of emission [*Jeong*, 2008; *Scheuvens et al.*, 2013], on wind speed [*Laurent et al.*, 2008] and on physical and chemical aging during transport [*Schütz et al.*, 1981; *Sullivan et al.*, 2007].

A "dynamic" representation of dust optical properties as a function of the physicochemical properties of particles is thus necessary not only to evaluate the magnitude of the dust longwave effect at the global scale but also to represent it in climate models and satellite retrieval schemes.

Since the 1970s, the technique most commonly used to estimate dust optical properties in the longwave has been the spectroscopy pellet technique, in which particles are dispersed and pressed in a KBr pellet and their reflectance or absorption spectra are measured. Spectra are then analyzed by means of an assumed optical theory to obtain the complex refractive indices of particles [*Mooney and Knacke*, 1985; *Sokolik et al.*, 1993]. The very few existing data on the absorption spectra and refractive indices obtained from measurements on natural samples indicate that the dust longwave optical properties largely vary depending on the physicochemical properties of particles [*Volz*, 1972, 1973; *Fouquart et al.*, 1987]. However, measurements with the pellet technique are performed on a single collection of particles with a single set of physicochemical properties and thus represent a "static" picture of the refractive index specific for that aerosol condition. Consequently, data from different studies are difficult to compare and the individual effects of composition, size, and shape on the particle optical properties are impossible to evaluate. Moreover, as the pellet technique requires one to mix the dust sample with KBr and then press the mixture to form the pellet, the size distribution of the analyzed sample may be inherently different from that of ambient dust aerosol.

The capability of providing a dynamic characterization of the dust optical properties requires performing measurements with a defined and reproducible protocol, in an environment in which the physicochemical properties of particles can be actively varied. This implies making use of a laboratory simulation chamber where atmospheric conditions can be reproduced and particles can be generated, processed, and deposited under controlled conditions and where the physicochemical properties and longwave spectra of particles can be measured simultaneously.

In this paper we present the first results of newly designed dust experiments conducted in the large volume (4.2 m^3) multiinstrumented CESAM atmospheric chamber (French acronym for Experimental Multiphasic Atmospheric Simulation Chamber) [*Wang et al.*, 2011]. The novelty of our experimental approach resides in the fact that the longwave extinction spectra are measured in situ using polydispersed mineral dust particles generated using a technique designed to mimic the sandblasting process responsible for the generation of dust in the real environment [*Alfaro and Gomes*, 2001]. This process results in the production of supermicron dusts, including particles as large as ~20 μm, which are the most efficient in interacting with longwave radiation. Compared to previous chamber studies, which have mostly looked at monodispersed submicron individual minerals (often synthetic) [*Hudson et al.*, 2008; *Mogili et al.*, 2007; *Laskina et al.*, 2012], this approach allows us to investigate dust-radiation interactions under more realistic conditions.

We conducted experiments on dust aerosols generated from parent soils collected from major global source regions in the African Sahara and Sahel, and the Asian Gobi desert, each of which is characterized by different mineralogical compositions. Dust aerosols are injected into CESAM at high concentrations (up to ~1000 μg m^{-3}), and then particles are left to sediment in the chamber until they reach <50–100 μg m^{-3}. At the same time, the evolution of their extinction spectra is measured with a Fourier transform infrared (FTIR) spectrometer. These conditions allow us to investigate the longwave extinction under conditions nearly equivalent to those ranging from dust storms nearby sources to transported plumes (aerosol longwave optical depths from ~2 to ~0.2) [*Highwood et al.*, 2003; *Turner*, 2008].

2. Experimental Setup

The schematic configuration of the CESAM setup for the dust experiments is shown in Figure S1 in the supporting information. Prior to each experiment, the chamber is evacuated and kept at the pressure of 10^{-4} mbar. Then, the reactor is filled at one atmosphere with a mixture of 80% N$_2$ and 20% O$_2$. Temperature and relative humidity are maintained constant at 293 K and <2% (Vaisala probe HMP234), respectively, during all experiments.

As described in *Alfaro et al.* [2004], dust aerosols are generated by mechanical shaking of natural soil samples, which reproduces the saltation and sandblasting processes responsible for the release of mineral dust in natural conditions. Approximately 60 g of soil and 60 g of pure quartz (Fontainebleau, France) are placed in a Buchner flask. The flask is first purged with pure N$_2$ (Linde, nitrogen 4.5) for ~3–5 min to eliminate gaseous impurities; then, the soil/quartz mixture is shaken for 30 min at 100 Hz using a sieve shaker (Retsch AS200). The presence of the pure quartz grains increases the efficiency of the saltation/sandblasting process thus allowing a rapid generation of high dust concentrations. The suspension of dust particles released from the

soil in the Buchner flask is then injected into the CESAM chamber over a period of 10–15 min by flushing the flask with N_2 at 10 L min^{-1}. Before entering CESAM, the air flow passes through a stainless steel cylinder of 61 cm height and 14 cm of diameter to remove, by gravitational settling, particles larger than ~15 μm at 50% efficiency, so to prevent any large quartz grains from entering the CESAM chamber. All connections are made using 1/2 inch silicon tubing (TSI Inc.), which minimizes particle loss via electrostatic deposition.

The suspension and homogeneity of the dust aerosols within the chamber is ensured by circulating the air using a four-wing stainless steel fan (32 cm diameter) operating at 600 rpm located at the bottom of the chamber.

Dust extinction spectra between 2.0 μm (5000 cm^{-1}) and 16.0 μm (625 cm^{-1}) are measured in situ in CESAM by a Fourier transform infrared (FTIR) spectrometer (Bruker® Tensor 37^{TM}) interfaced with a multipass cell. The spectrometer is equipped with a liquid nitrogen-cooled Mercury Cadmium Telluride detector and a Globar source. The multipass cell, which consists of three high reflectivity gold-coated mirrors with a base length of 2 m, is adjusted to achieve a total path length of (192 ± 4) m. The IR beam enters and exits the reactor by passing through ZnSe windows. Measurements are performed at 1 cm^{-1} resolution by coadding 158 scans over 2 min. The FTIR reference spectrum is acquired immediately before dust injection. Small amounts of water vapor and CO_2 in some cases entered CESAM during particle injection and partly contaminated the dust spectra below 7 μm. This does not influence the state of particles as the chamber atmosphere remained very dry (relative humidity $< 2\%$). Gas lines are removed by means of an automated software optimization routine; then the spectra are interpolated at 0.02 μm wavelength resolution.

Particle number size distributions are acquired simultaneously with FTIR spectra from two Grimm® optical particle sizers (OPS, Grimm Inc., model 1.109; 655 nm operating wavelength) working in the diameter range 0.25–32 μm. The OPS sphere-equivalent optical diameters have been converted into sphere-equivalent geometrical diameters (D_g) by taking into account the dust complex refractive index [*Liu and Daum*, 2000]. In the absence of an independent estimate of the dust refractive index at 655 nm, the optical to geometrical diameter conversion has been performed based on the range of values reported in the literature for dust at visible wavelengths, i.e., $n_{vis} = 1.42$–1.56, with a mean of ~1.53 for the real part, and $k_{vis} = 0.001$–0.005 for the imaginary part [*Osborne et al.*, 2008; *Petzold et al.*, 2009; *McConnell et al.*, 2010; *Klaver et al.*, 2011]. Optical calculations are computed using Mie theory for $n_{vis} = 1.42$, 1.53, and 1.56 by varying k_{vis} at step of 0.001 between 0.001 and 0.005. D_g has then been set at the mean $\pm$ one standard deviation of the values obtained for the different n_{vis} and k_{vis}. After conversion, the OPS diameter range became 0.28–72.2 μm with an associated uncertainty between 3 and 11.5%.

One of the two OPS intakes was placed on the same horizontal plane as the FTIR spectrometer, while the second was placed ~50 cm below the FTIR level and at ~60 cm across the chamber from the first OPS. This arrangement was chosen to monitor possible inhomogeneity of the dust distribution within the chamber. Differences between the two OPS are consistently below 10%, which indicates that the dust distribution within the chamber is homogeneous. For the sake of clarity, only the measurements from the OPS located at the same height as the FTIR will be shown.

The natural soil samples used in this study to generate dust correspond to the first few millimeters of soil which, in the real world, is the fraction subject to wind erosion. They were collected in the field with special care using a plastic shovel; after collection, they were stored in plastic containers [see also *Alfaro et al.*, 2004 and *Lafon*, 2004]. For this first study, we have selected three soils representative of some of the major global source areas worldwide:

1. A soil from Niger, representative of the African Sahel, collected at the rural site of Banizoumbou (13°31′N, 2°38′E). Dust emitted from the Sahel participates in long-range transport at the intercontinental scale across the North Atlantic Ocean [e.g., *Reid et al.*, 2003].
2. A soil from Tunisia, representative of the northern Sahara. This soil was collected in the southern part of Tunisia, at Maouna (33°01′N, 10°40′E). This is a source region for dust transported toward Europe across the Mediterranean [e.g., *Prodi and Fea*, 1979].
3. A soil from the Ulan Buh area (39°26′N, 105°40′E) in the Chinese Gobi desert. This is a major source area in China, accounting for infrequent but extremely intense emissive events, which then are transported over severely polluted high-density urban areas [*Lu et al.*, 2010].

These soils, and so the corresponding aerosols, differ in their chemical and mineralogical compositions, as analyzed in *Lafon* [2004] and *Lafon et al.* [2006]. The Niger soil is rich in quartz and kaolinite clay, contains
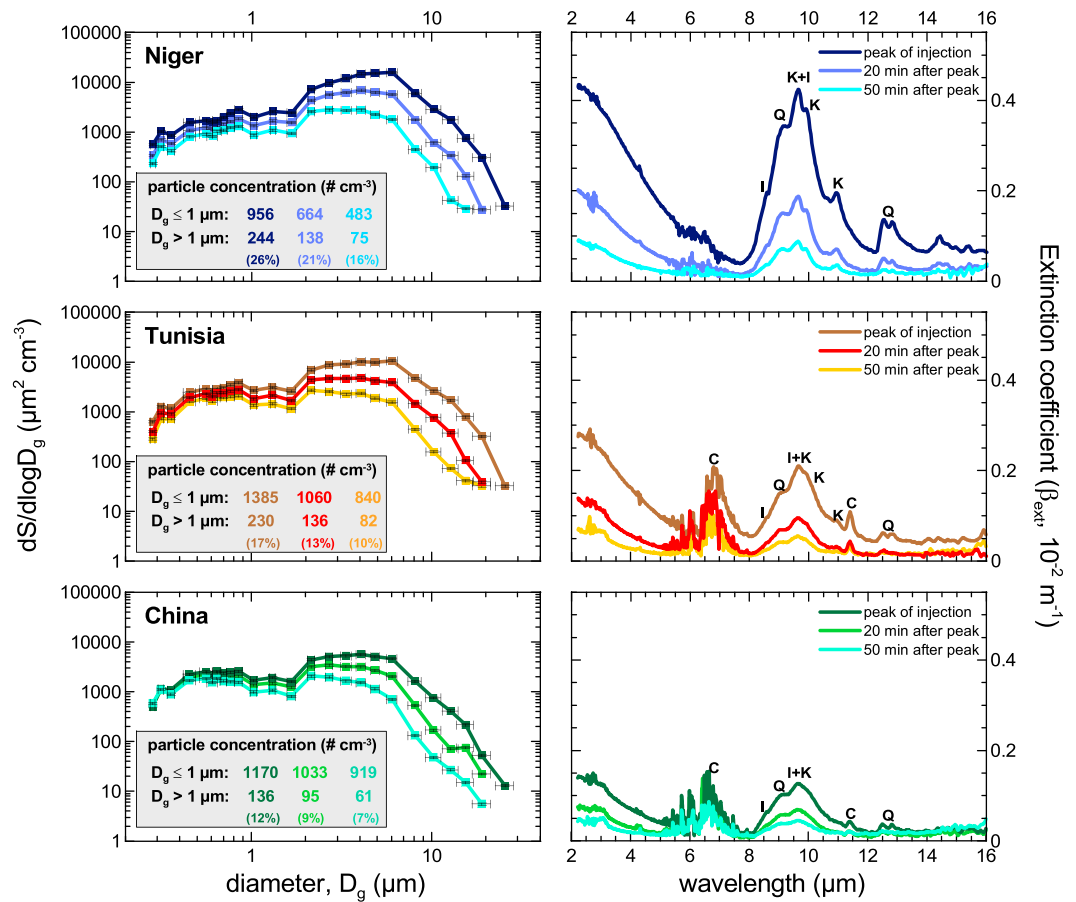
Figure 1. (left) Surface size distributions (2 min averages) and (right) extinction spectra ($\beta_{ext}(\lambda)$) for the Niger, Tunisia, and China aerosols taken at the peak of the dust injection and at 20 and 50 min after the peak. Error bars on the size plots correspond to the uncertainty associated with the optical to geometrical diameter conversion (*x* error) and the standard deviation over the 2 min average (*y* error, ~5%). The total submicron ($D_g \leq 1 \mu m$) and supermicron ($D_g > 1 \mu m$) particle concentrations, as well as the percentage of the supermicron to submicron fractions (values in parentheses), are reported. Main absorption bands by quartz (Q), kaolinite (K), illite (I), and calcite (C) are also indicated in the β_{ext} spectra.

minor quantities of illite, and presents no traces of calcite; the Tunisian soil is very rich in calcite, enriched in illite with respect to kaolinite, and presents traces of quartz; the Chinese soil is rich in illite and presents traces of calcite but contains little quartz and kaolinite. Prior to use in CESAM, all soils were sieved to less than 1000 μm to eliminate any nonerodable grains. Information on samples analyzed in this study are provided in the supporting information (Table S1).

3. Results

Figure 1 shows the surface area size distribution ($\mu m^2 \, cm^{-3}$) and extinction coefficient ($\beta_{ext}(\lambda)$, [m^{-1}]) spectra obtained for the Niger, Tunisia, and China dust aerosols at the peak of the dust injection, i.e., at the maximum of the measured particle mass concentration and at 20 and 50 min after the peak. The dust extinction coefficient was estimated from FTIR-measured spectral transmittance, $T(\lambda)$, using the following equation:

$$\beta_{ext}(\lambda) = -\ln(T(\lambda))x^{-1} \tag{1}$$

where x is the total optical path within the chamber, (192 ± 4) m. The $\beta_{ext}(\lambda)$ uncertainty, obtained by combining the uncertainties on $T(\lambda)$ (~1% noise) and x, is ~5%.

The dust mass concentration estimated from the OPS data (dust density set at 2.5 g cm^{-3}) at the three selected times varies between ~800–1200, 300–500, and 100–200 μg m^{-3}. The dust size distributions present multimodal structures with main modes centered at ~0.3, 0.5, 0.8, 1.5, 2, 6, and 13 μm. The size distributions

for the three aerosol samples are very similar, which indicates that the dust laboratory generation procedure is quite reproducible. The size distributions obtained here compare well with dust field observations from several airborne campaigns in Africa and Asia, as shown in Figure S2. By assuming a transport height of 3 km, which is a characteristic for the Saharan Air Layer [*Karyampudi et al.*, 1999], and a mean particle dry deposition velocity of 1 cm s^{-1} [*Seinfeld and Pandis*, 2006], the depletion ratio obtained for particles of 10 μm diameter at 50 min would correspond to an atmospheric residence time of 5–6 days, which is a time scale typical of long-range intercontinental transport [*Reid et al.*, 2003].

The extinction spectra displayed in Figure 1 clearly show the contribution of dust scattering between 2 and 8 μm; above 8 μm, however, extinction is dominated by absorption. In this wavelength region, significant differences are observed in the spectra of the three dust samples. These, in turn, are associated with the differences in their mineralogical composition:

1. Niger aerosols, which are enriched in quartz and kaolinite, show strong absorption bands at 9.2 μm and 12.5–12.9 μm, and ~10 and 11 μm, respectively. A pronounced peak at 9.6 μm, due to the combination of kaolinite and illite absorptions, as well as a small peak at 8.6 μm due to illite, is also present in the measured spectra.
2. Tunisia aerosols have an elevated content of calcite, which absorbs strongly at ~7 and 11.4 μm, and show clear signatures due to illite and kaolinite (8.6, 9.6, 10, 11 μm) and, in minor fraction, quartz (9.2, 12.5–12.9 μm).
3. China dusts, which are dominated by illite, present main clay absorption bands at 8.6 and 9.6 μm. Clear signatures due to calcite (7, 11.4 μm) and, to a lesser extent, quartz (9.2, 12.5–12.9 μm) are also detected.

The intensities of the dust extinction spectra depend strongly on the particle size distribution and in particular on the contribution from the aerosol supermicron fraction. For instance, the highest values (~0.45 × 10^{-2} m^{-1}) of both dust scattering below 8 μm and absorption in the 8–12 μm window spectral region are observed for the Niger aerosols, which are also the richest in supermicron particles (26% in number at the peak of the injection compared to the 17% and 12% for Tunisia and China aerosols). The spectral intensities rapidly decrease after injection, following the decrease of the supermicron number/mass particle concentration. The extinction spectra intensities are about halved after 20 min and reduced to 20–30% of their initial values after 50 min. The evolution of the dust extinction spectra with time as shown in these experiments may be taken as indicative of the changes which may occur during medium- and long-range transport if dry deposition is the dominant process.

An optical inversion procedure was applied to retrieve the dust longwave complex refractive index ($m = n - ik$) from the size and extinction data obtained simultaneously in CESAM. Starting from the measured number size distribution, $dN/dlogD_g$, the extinction coefficient, $\beta_{ext}(\lambda)$ can be recalculated as

$$(\beta_{ext}(\lambda))_{calc} = \sum_{D_g} \frac{\pi D_g^2}{4} Q_{ext}(m, \lambda, D_g) \frac{dN}{dlogD_g} dlogD_g \tag{2}$$

where $Q_{ext}(m, \lambda, D_g)$ is the particle extinction efficiency. As the simplest approach, Q_{ext} is computed using Mie theory for spherical particles. Our retrieval algorithm consists of iteratively varying m in expression (2) until $(\beta_{ext}(\lambda))_{calc}$ matches the measured $\beta_{ext}(\lambda)$. However, as m is a complex number with two variables, an additional condition is needed. According to the electromagnetic theory, n and k must satisfy the Kramers-Kronig (K-K) relation [*Bohren and Huffman*, 1983]:

$$n(\omega) - 1 = \frac{2}{\pi} p \int_0^\infty \frac{\Omega \cdot k(\Omega)}{\Omega^2 - \omega^2} \cdot d\Omega \tag{3}$$

with ω the angular frequency of radiation ($\omega = 2\pi c/\lambda$, [s^{-1}]) and P the principal value of the Cauchy integral. Equation (3) means that if $k(\lambda)$ is known, then $n(\lambda)$ can be calculated accordingly. Hence, K-K equation (3) is the additional condition besides (2) to retrieve n and k. A direct calculation of the K-K integral is, however, very difficult as it requires the knowledge of k over an infinite wavelength range. A useful formulation which permits to obtain *n-k* values which automatically satisfy the K-K condition is the one based on the Lorentz

dispersion theory. In the Lorentz formulation, n and k may be written as a function of the real (ε_r) and imaginary (ε_i) parts of the particle dielectric function as

$$n(\omega) = \left(\frac{1}{2} \left[\sqrt{(\varepsilon_r(\omega))^2 + (\varepsilon_i(\omega))^2} + \varepsilon_r(\omega) \right] \right)^{1/2} \tag{4a}$$

$$k(\omega) = \left(\frac{1}{2} \left[\sqrt{(\varepsilon_r(\omega))^2 + (\varepsilon_i(\omega))^2} - \varepsilon_r(\omega) \right] \right)^{1/2} \tag{4b}$$

$\varepsilon_r(\omega)$ and $\varepsilon_i(\omega)$ can be in turn expressed as the sum of N Lorentzian harmonic oscillators:

$$\varepsilon_r(\omega) = \varepsilon_\infty + \left[\sum_{j=1}^{N} \frac{F_j\left(\omega_j^2 - \omega^2\right)}{\left(\omega_j^2 - \omega^2\right)^2 + \gamma_j^2 \omega^2} \right] \tag{5a}$$

$$\varepsilon_i(\omega) = \sum_{j=1}^{N} \frac{F_j \gamma_j \omega}{\left(\omega_j^2 - \omega^2\right)^2 + \gamma_j^2 \omega^2} \tag{5b}$$

where $\varepsilon_{vis} = n_{vis}^2$ is the real dielectric function in the limit of visible wavelengths and (ω_j, γ_j, F_j) are the three parameters (i.e., eigenfrequency, damping factor, and strength) characterizing the jth oscillator. In our algorithm we combine (4a)–(4b) and (5a)–(5b) with (2) to retrieve n-k values which allow both to reproduce the measured $\beta_{ext}(\lambda)$ and to satisfy the K-K relation. In practice, in the iteration procedure only one of the two components of the refractive index (in our case, k) is varied, while the other (n) is recalculated at each step based on the values of the oscillator parameters (ω_j, γ_j, F_j) obtained from a best fit of k. n_{vis}, i.e., the dust real component of the refractive index at visible wavelengths, in (5a) is manually varied and fixed to the value which allows for a better reproduction of the dust scattering signal below 8 μm. The resulting n_{vis} is 1.35 for the Niger dust and 1.32 for Tunisia and China aerosols. Additional details and the flowchart of the refractive index retrieval procedure are provided in Text S1 and Figure S3.

A sensitivity analysis was performed to assign an uncertainty to the retrieved refractive indices. To this purpose, n and k are also obtained by using as input to the retrieval algorithm the measured size distribution and $\beta_{ext}(\lambda) \pm$ their estimated uncertainties. The deviations of the values of n and k retrieved in the sensitivity study with respect to those obtained in the first inversion are assumed to correspond to the one standard deviation uncertainty. The results indicate that the main source of uncertainty for n and k retrieval is the optical to geometrical diameter conversion error on the size distribution (± 20–60% estimated uncertainty at 8–12 μm), while the y errors on dN/dlogD_g and $\beta_{ext}(\lambda)$ have a smaller impact on the retrieved refractive index ($< \pm 10$–15%). Other sources of uncertainty, which we do not quantify here, include the use of Mie theory to calculate $\beta_{ext}(\lambda)$ in the inversion procedure and the choice of the n_{vis} value.

The real and imaginary parts of the complex refractive index obtained in the range 6–14 μm for the Niger, Tunisia, and China aerosols are shown in Figure 2. For each dust type, estimates of n and k at the three selected times (see Figure S4 in the supporting information) are observed to agree within error bars, consistently with the fact that the dust composition is dominated by clays and does not change significantly with time.

As a consequence of their differing mineralogies, the imaginary part of the refractive index varies significantly in magnitude for the Niger, Tunisia, and China aerosols. The largest differences are observed in the 8.5–10 μm range between the Niger dust ($k \sim 0.3$–0.9) and Tunisia and China dusts ($k \sim 0.15$–0.5 and $k \sim 0.3$–0.65, respectively). This is mainly linked to the highest content in the Nigerian aerosols of quartz and kaolinite, highly absorbing at these wavelengths, compared to Tunisian and Chinese dusts, which are poorer in these minerals. Conversely, Tunisia and China aerosols show a very intense calcite-associated peak at 7 μm, which is not present in the k spectrum of Niger dust. Minor but detectable differences in the k spectra of the three samples curves are also present above 11 μm; these are attributable to minor absorption features of kaolinite, calcite, and quartz.

The real part of the dust refractive index varies in the range 0.6–1.7 and presents its main signatures in correspondence of the absorption bands of clays and quartz at 8.5–10 μm, and calcite at 7 μm. The spectral behavior of n is very similar for the Tunisian and Chinese dusts throughout the whole considered range, while differences are observed with the Nigerian spectra especially below 12 μm.
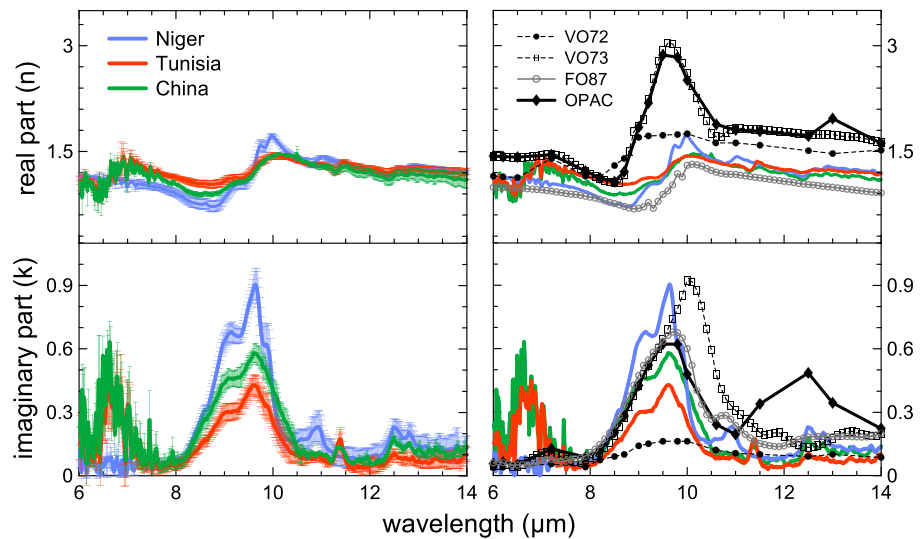
Figure 2. (left) Real and imaginary parts of the complex refractive index obtained in the range 6–14 μm, including the atmospheric window, for the Niger, Tunisia, and China aerosols. The curves correspond to the mean and the standard deviation of the values obtained at the peak of the dust injection and 20 and 50 min after the peak. (right) Comparison between our results and estimates of the dust refractive index from *Volz* [1972] (VO72, rainout dust aerosols collected in Germany), *Volz* [1973] (VO73, Saharan dust collected at Barbados, West Indie), *Fouquart et al.* [1987] (FO87, Sahelian sand collected at Niamey, Niger), and the OPAC desert model [*Hess et al.*, 1998].

In Figure 2, we compare the results of our analysis with values of the dust refractive index from *Volz* [1972, 1973] and *Fouquart et al.* [1987] (obtained from pellet transmission measurements on natural dust samples) and the values of the OPAC (Optical Properties of Aerosols and Clouds) database [*Hess et al.*, 1998]. We selected these studies because they are among the most widely used references in atmospheric and climatic studies, as well as in satellite inversion algorithms [*Klüser et al.*, 2012].

The best agreement between CESAM and literature data is found with the measurements of *Fouquart et al.* [1987] for Sahelian dust, which on average better reproduce the magnitude of n and k in the whole range of wavelengths as obtained in our study (reduced $\chi^2 \sim 2$–43 for the different cases). Aside a poor spectral resolution, *Fouquart et al.* [1987] show in their k a clear signature due to kaolinite absorption at 11 μm, which we also observe in our Niger sample. A relative good agreement, only in the real part, is also obtained for Tunisia and China dust below 7 μm with data from *Volz* [1972], which reproduce the signature of calcite at these wavelengths. A relatively weak correlation ($\chi^2 \sim 7$–22) is instead observed between our data and the data from *Volz* [1973] above ~8–9 μm, predominantly due to the shift of main clay absorption band at ~10 μm for this data set, and with OPAC ($\chi^2 \sim 8$–41) mainly above 11 μm, due to the strong contribution of quartz assumed in this dust model.

Our results show clear signatures of the main mineral components of the different dusts. These signatures are not so apparent in the older studies shown in Figure 2. In particular, clay and quartz bands appear strongly smoothed in the 8 and 11 μm region, where the maximum dust absorption is found. The quartz signal at 12.5–12.9 μm is not accurately estimated in all data sets (underestimated in all studies with the exception of OPAC where it is considerably overestimated). The calcite band at 7 μm, as well as the small peak at 11.4 μm, whose contribution is of primary relevance for both Tunisia and China cases, is not at all present in the considered k reference data.

4. Conclusions and Perspectives

In this paper, we present the first in situ laboratory measurements of the longwave extinction spectra and derived imaginary part of the complex refractive index of natural polydispersed dust particles from major source regions in Africa and Asia.

The experiments were conducted in the CESAM chamber, which is characterized by a long optical path length (~192 m), an optimized dust generation system, and a particle lifetime comparable to that of dust in the atmosphere. This unique setup permits to measure dust extinction in a nearly realistic and dynamic

environment, well representative of natural conditions. Owing to these features, the measured extinction spectra and dust refractive indices, made available as supporting information to this paper, are readily usable in radiative transfer and remote sensing applications without assumptions regarding particle size distribution and composition or corrections for multiple scattering.

Our results for African and Asian dusts show that extinction spectra and refractive indices significantly vary as a function of particle origin and suggest that available literature data do not adequately represent this variability. Furthermore, our observation that the extinction signal persists down to low coarse particle fractions indicates that the dust-induced longwave radiative perturbation can be significant even for long-range transported dust and is potentially relevant at the global scale.

Given these results, we suggest that both in satellite retrievals and in climate studies, research should move from the use of a single global value of the refractive index (commonly that of the OPAC database) toward the use of regionally resolved values [*Klüser et al.*, 2012; *Colarco et al.*, 2014]. For the Saharan and the Gobi desert aerosols, for instance, we estimate lower absorption that in the OPAC database. *Colarco et al.* [2014] have recently shown that this lower absorption would reduce the top-of-atmosphere and surface longwave dust radiative effect (all-sky) at the global scale. The results of our study clearly respond to the evidence highlighted by these authors regarding the importance of better constraining the dust refractive index in order to improve our modeling capability.

In addition, our data show very complex signatures of the extinction and refractive index spectra of dust, which are only in minor part reproduced in the coarse resolved OPAC model. A better spectral characterization of the dust optical properties is thus required to improve satellite retrievals, in particular for the new generation of very high resolution infrared sounders, i.e., the Atmospheric Infrared Sounder (AIRS) and the Infrared Atmospheric Sounding Interferometer (IASI) [*Klüser et al.*, 2011].

This work represents a first step toward the provision of the dust regionally resolved and high-resolution refractive index data needed by climate and satellite applications. The approach and the results obtained here are promising, since we are able to resolve the main features of the dust refractive index as well as the differences between diverse source areas. However, two main aspects of the refractive index retrieval algorithm need to be improved to obtain more stable and constrained solutions. The first consists in providing an independent estimation of n_{vis}, necessary both to correct the size distribution measurements in a more precise way and to force the $n(\lambda)$ retrieval at low wavelengths. The second concerns the necessity of using, in place of the Mie theory, an optical model adapted to the irregular shape of dust particles. These issues will be investigated in future works to increase the accuracy and the applicability of our results.

References

Alfaro, S. C., and L. Gomes (2001), Modeling mineral aerosol production by wind erosion: Emission intensities and aerosol distributions in source areas, *J. Geophys. Res.*, *106*(D16), 18,075–18,084, doi:10.1029/2000JD900339.

Alfaro, S. C., S. Lafon, J. L. Rajot, P. Formenti, A. Gaudichet, and M. Maillé (2004), Iron oxides and light absorption by pure desert dust: An experimental study, *J. Geophys. Res.*, *109*, D08208, doi:10.1029/2003JD004374.

Balkanski, Y., M. Schulz, T. Claquin, and S. Guibert (2007), Reevaluation of mineral aerosol radiative forcings suggests a better agreement with satellite and AERONET data, *Atmos. Chem. Phys.*, *7*, 81–95, doi:10.5194/acp-7-81-2007.

Bohren, C. E., and D. R. Huffman (1983), *Absorption and Scattering of Light by Small Particles*, Wiley, New York.

Claquin, T., M. Schulz, Y. J. Balkanski, and O. Boucher (1998), Uncertainties in assessing radiative forcing by mineral dust, *TellusB*, *50*, 491–505.

Colarco, P. R., E. P. Nowottnick, C. A. Randles, B. Yi, P. Yang, K.-M. Kim, J. A. Smith, and C. G. Bardeen (2014), Impact of radiatively interactive dust aerosols in the NASA GEOS-5 climate model: Sensitivity to dust particle shape and refractive index, *J. Geophys. Res. Atmos.*, *119*, 753–786, doi:10.1002/2013JD020046.

di Sarra, A., C. Di Biagio, D. Meloni, F. Monteleone, G. Pace, S. Pugnaghi, and D. Sferlazzo (2011), Shortwave and longwave radiative effects of the intense Saharan dust event of March 25–26, 2010, at Lampedusa (Mediterranean sea), *J. Geophys. Res.*, *116*, D23209, doi:10.1029/2011JD016238.

Fouquart, Y., B. Bonnel, G. Brogniez, J. C. Buriez, L. Smith, and J. J. Morcrette (1987), Observations of Sahara aerosols: Results of ECLATS field experiment. Part II: Broadband radiative characteristics of the aerosols and vertical radiative flux divergence, *J. Clim. Appl. Meteorol.*, *26*, 38–52.

Haywood, J. M., et al. (2011), Motivation, rationale and key results from the GERBILS Saharan dust measurement campaign, *Q. J. R. Meteorol. Soc.*, *137*, 1106–1116.

Hess, M., P. Koepke, and I. Schult (1998), Optical properties of aerosols and clouds: The software package OPAC, *Bull. Am. Meteorol. Soc.*, *79*, 831–844.

Highwood, E. J., J. M. Haywood, M. D. Silverstone, S. M. Newman, and J. P. Taylor (2003), Radiative properties and direct effect of Saharan dust measured by the C-130 aircraft during Saharan Dust Experiment (SHADE): 2. Terrestrial spectrum, *J. Geophys. Res.*, *108*(D18), 8578, doi:10.1029/2002JD002552.

Hsu, N. C., J. R. Herman, and C. J. Weaver (2000), Determination of radiative forcing of Saharan dust using combined TOMS and ERBE data, *J. Geophys. Res.*, *105*(D16), 20,649–20,661, doi:10.1029/2000JD900150.

DI BIAGIO ET AL.   6296

Hudson, P. K., E. R. Gibson, M. A. Young, P. D. Kleiber, and V. H. Grassian (2008), Coupled infrared extinction and size distribution measurements of several clay components of mineral dust aerosol, *J. Geophys. Res.*, *113*, D01201, doi:10.1029/2007JD008791.

Jeong, G. Y. (2008), Bulk and single-particle mineralogy of Asian dust and a comparison with its source soils, *J. Geophys. Res.*, *113*, D02208, doi:10.1029/2007JD008606.

Karyampudi, V. M., et al. (1999), Validation of the Saharan dust plume conceptual model using lidar, Meteosat, and ECMWF data, *Bull. Am. Meteorol. Soc.*, *80*, 1045–1075.

Klaver, A., P. Formenti, S. Caquineau, S. Chevaillier, P. Ausset, G. Calzolai, S. Osborne, B. Johnson, M. Harrison, and O. Dubovik (2011), Physico-chemical and optical properties of Sahelian and Saharan mineral dust: In situ measurements during the GERBILS campaign, *Q. J. R. Meteorol. Soc.*, *137*, 1193–1210, doi:10.1002/qj.889.

Klüser, L., D. Martynenko, and T. Holzer-Popp (2011), Thermal infrared remote sensing of mineral dust over land and ocean: a spectral SVD based retrieval approach for IASI, *Atmos. Meas. Tech.*, *4*, 757–773, doi:10.5194/amt-4-757-2011.

Klüser, L., P. Kleiber, T. Holzer-Popp, and V. H. Grassian (2012), Desert dust observation from space—Application of measured mineral component infrared extinction spectra, *Atmos. Environ.*, *54*, 419–427, doi:10.1016/j.atmosenv.2012.02.011.

Lafon, S. (2004), Les oxides de fer dans l'aerosol desertique en relation avec ses proprietes optiques: Caracterisation physico-chimique de poussieres minerales generees en soufflerie, PhD thesis, Univ. Paris XII, Paris, France.

Lafon, S., I. N. Sokolik, J. L. Rajot, S. Caquineau, and A. Gaudichet (2006), Characterization of iron oxides in mineral dust aerosols: Implications for light absorption, *J. Geophys. Res.*, *111*, D21207, doi:10.1029/2005JD007016.

Laskina, O., M. A. Young, P. D. Kleiber, and V. H. Grassian (2012), Infrared extinction spectra of mineral dust aerosol: Single components and complex mixtures, *J. Geophys. Res.*, *117*, D18210, doi:10.1029/2012JD017756.

Laurent, B., B. Marticorena, G. Bergametti, J. F. Léon, and N. Mahowald (2008), Modeling mineral dust emissions from the Sahara desert using new surface properties and soil database, *J. Geophys. Res.*, *113*, D14218, doi:10.1029/2007JD009484.

Liu, Y., and P. Daum (2000), The effect of refractive index on size distributions and light scattering coefficients derived from optical particle counters, *J. Aerosol Sci.*, *31*, 945–957, doi:10.1016/S0021-8502(99)00573-X.

Lu, Z., D. G. Streets, Q. Zhang, S. Wang, G. R. Carmichael, Y. F. Cheng, C. Wei, M. Chin, T. Diehl, and Q. Tan (2010), Sulfur dioxide emissions in China and sulfur trends in East Asia since 2000, *Atmos. Chem. Phys.*, *10*(13), 6311–6331, doi:10.5194/acp-10-6311-2010.

May, D. A., L. L. Stowe, J. D. Hawkins, and E. P. McClain (1992), A correction for Saharan dust effects on satellite sea surface temperature measurements, *J. Geophys. Res.*, *97*(C3), 3611–3619, doi:10.1029/91JC02987.

McConnell, C. L., P. Formenti, E. J. Highwood, and M. A. Harrison (2010), Using aircraft measurements to determine the refractive index of Saharan dust during the DODO Experiments, *Atmos. Chem. Phys.*, *10*, 3081–3098, doi:10.5194/acp-10-3081-2010.

Merchant, C. J., O. Embury, P. Le Borgne, and B. Bellec (2006), Saharan dust in nighttime thermal imagery: Detection and reduction of related biases in retrieved sea surface temperature, *Remote Sens. Environ.*, *104*(1), 15–30, doi:10.1016/j.rse.2006.03.007.

Mogili, P. K., K. H. Yang, M. A. Young, P. D. Kleiber, and V. H. Grassian (2007), Environmental aerosol chamber studies of extinction spectra of mineral dust aerosol components: Broadband IR-UV extinction spectra, *J. Geophys. Res.*, *112*, D21204, doi:10.1029/2007JD008890.

Mooney, T., and R. F. Knacke (1985), Optical constants of chlorite and serpentine between 2.5 and 50 μm, *Icarus*, *64*, 493–502, doi:10.1016/0019-1035(85)90070-3.

Osborne, S. R., B. T. Johnson, J. M. Haywood, A. J. Baran, M. A. J. Harrison, and C. McConnell (2008), Physical and optical properties of mineral dust aerosol during the dust and biomass-burning experiment, *J. Geophys. Res.*, *113*, D00C03, doi:10.1029/2007JD009551.

Petzold, A., et al. (2009), Saharan dust absorption and refractive index from aircraft-based observations during SAMUM 2006, *Tellus B*, *61*, 118–130, doi:10.1111/j.1600-0889.2008.00383.x.

Prodi, F., and G. Fea (1979), A case of transport and deposition of Saharan dust over the Italian peninsula and southern Europe, *J. Geophys. Res.*, *84*, 6951–6960, doi:10.1029/JC084iC11p06951.

Reid, E. A., J. S. Reid, M. M. Meier, M. R. Dunlap, S. S. Cliff, A. Broumas, K. Perry, and H. Maring (2003), Characterization of African dust transported to Puerto Rico by individual particle and size segregated bulk analysis, *J. Geophys. Res.*, *108*(D19), 8591, doi:10.1029/2002JD002935.

Scheuvens, D., L. Schütz, K. Kandler, M. Ebert, and S. Weinbruch (2013), Bulk composition of northern African dust and its source sediments— A compilation, *Earth Sci. Rev.*, *116*, 170–194, doi:10.1016/j.earscirev.2012.08.005.

Schütz, L., R. Jaenicke, and H. Pietrek (1981), Saharan dust transport over the North Atlantic Ocean, *Spec. Pap. Geol. Soc. Am.*, *186*, 87–100.

Seinfeld, J. H., and S. N. Pandis (2006), *Atmospheric Chemistry and Physics: From Air Pollution to Climate Change*, Wiley, New York.

Slingo, A., et al. (2006), Observations of the impact of a major Saharan dust storm on the atmospheric radiation balance, *Geophys. Res. Lett.*, *33*, L24817, doi:10.1029/2006GL027869.

Sokolik, I. N. (2002), The spectral radiative signature of wind-blown mineral dust: Implications for remote sensing in the thermal IR region, *Geophys. Res. Lett.*, *29*(24), 2154, doi:10.1029/2002GL015910.

Sokolik, I. N., A. Andronova, and T. C. Johnson (1993), Complex refractive index of atmospheric dust aerosols, *Atmos. Environ.*, *27A*, 2495–2502.

Sokolik, I. N., O. B. Toon, and R. W. Bergstrom (1998), Modeling the radiative characteristics of airborne mineral aerosols at infrared wavelengths, *J. Geophys. Res.*, *103*, 8813–8826, doi:10.1029/98JD00049.

Sokolik, I., and O. Toon (1999), Incorporation of mineralogical composition into models of the radiative properties of mineral aerosol from UV to IR wavelengths, *J. Geophys. Res.*, *104*, 9423–9444, doi:10.1029/1998JD200048.

Sullivan, R. C., S. A. Guazzotti, D. A. Sodeman, and K. A. Prather (2007), Direct observations of the atmospheric processing of Asian mineral dust, *Atmos. Chem. Phys.*, *7*, 1213–1236, doi:10.5194/acp-7-1213-2007.

Turner, D. D. (2008), Ground-based infrared retrievals of optical depth, effective radius, and composition of airborne mineral dust above the Sahel, *J. Geophys. Res.*, *113*, D00E03, doi:10.1029/2008JD010054.

Volz, F. E. (1972), Infrared refractive index of atmospheric aerosol substances, *Appl. Optics*, *11*, 755–759.

Volz, F. E. (1973), Infrared optical constants of ammonium sulfate, Sahara dust, volcanic pumice and flyash, *Appl. Optics.*, *12*, 564–568.

Wang, J., J. F. Doussin, S. Perrier, E. Perraudin, Y. Katrib, E. Pangui, and B. Picquet-Varrault (2011), Design of a new multi-phase experimental simulation chamber for atmospheric photosmog, aerosol and cloud chemistry research, *Atmos. Meas. Tech.*, *4*, 2465–2494, doi:10.5194/amt-4-2465-2011.